

# On the deceleration of FR I jets: mass loading by stellar-winds

M. Perucho<sup>1\*</sup>, J. M. Martí<sup>1</sup>, R. A. Laing<sup>2</sup>, P. E. Hardee<sup>3</sup>

<sup>1</sup>*Departament d'Astronomia i Astrofísica. Universitat de València. C/ Dr. Moliner 50, 46100 Burjassot (València), Spain*

<sup>2</sup>*European Southern Observatory, Karl-Schwarzschild-Strasse 2, D-85748 Garching-bei-München, Germany*

<sup>3</sup>*Department of Physics & Astronomy, The University of Alabama, Tuscaloosa, AL 35487, USA*

Released 2012 Xxxxx XX

## ABSTRACT

Jets in low-luminosity radio galaxies are known to decelerate from relativistic speeds on parsec scales to mildly or sub-relativistic speeds on kiloparsec scales. Several mechanisms have been proposed to explain this effect, including strong reconfinement shocks and the growth of instabilities (both leading to boundary-layer entrainment) and mass loading from stellar winds or molecular clouds. We have performed a series of axisymmetric simulations of the early evolution of jets in a realistic ambient medium to probe the effects of mass loading from stellar winds using the code *Ratpenat*. We study the evolution of Fanaroff-Riley Class I (FRI) jets, with kinetic powers  $L_j \sim 10^{41} - 10^{44} \text{ erg s}^{-1}$ , within the first 2 kpc of their evolution, where deceleration by stellar mass loading should be most effective. Mass entrainment rates consistent with present models of stellar mass loss in elliptical galaxies produce deceleration and effective decollimation of weak FRI jets within the first kiloparsec. However, powerful FRI jets are not decelerated significantly. In those cases where the mass loading is important, the jets show larger opening angles and decollimate at smaller distances, but the overall structure and dynamics of the bow-shock are similar to those of unloaded jets with the same power and thrust. According to our results, the flaring observed on kpc scales is initiated by mass loading in the weaker FRI jets and by reconfinement shocks or the growth of instabilities in the more powerful jets. The final mechanism of decollimation and deceleration is always the development of disruptive pinching modes.

**Key words:** galaxies: active – galaxies: jets – hydrodynamics – stars: winds, outflows

## 1 INTRODUCTION

Jets from radio-loud AGN show two characteristic morphologies, associated with the FRI and FRII classes defined by Fanaroff & Riley (1974). Jets in FRI sources (e.g., 3C 31, Laing & Bridle 2002a) expand rapidly on kiloparsec scales, whereas those in the more powerful FRII sources (e.g., Cyg A, Carilli & Barthel 1996) are highly collimated until they terminate in compact hot-spots. FRI and FRII jets appear morphologically similar on parsec scales and both show evidence for relativistic speeds, although the former appear to be somewhat slower and to have significant velocity gradients (Giovannini et al. 2001; Celotti & Ghisellini 2008; Meyer et al. 2011). The current paradigm for FRI jets is that, unlike FRII jets, they are decelerated by entrainment of gas (Bicknell 1984; Laing 1993, 1996). Whether this susceptibility to entrainment is solely a function of the power

of the jet and its external environment or is due to a more fundamental difference is currently a matter of debate.

Two main processes have been invoked to explain entrainment in FRI jets: (i) mixing in a turbulent shear layer between the jet and the ambient (De Young 1986, 1993; Bicknell 1994; Wang et al. 2009), and (ii) injection from stellar mass loss (Phinney 1983; Komissarov 1994; Bowman et al. 1996; Laing & Bridle 2002b; Hubbard & Blackman 2006). Concerning the process of entrainment through a turbulent shear layer, Perucho & Martí (2007, hereafter PM07) showed, via a 2D axisymmetric simulation, that a recollimation shock in a light jet formed in reaction to steep interstellar density and pressure gradients may trigger nonlinear perturbations that lead to jet disruption and mixing with the external medium. Meliani, Keppens & Giacomazzo (2008) and Rossi et al. (2008) discussed the deceleration of FRI jets at discontinuities in the ambient medium and by the growth

\* E-mail: manel.perucho@uv.es

of helical instabilities in a jet propagating through a homogeneous ambient medium, respectively.

The influence of mass loading by stellar winds in FRI jets was studied by Komissarov (1994), who showed that this problem can be treated as a hydrodynamical one, as the gyroradii of the particles are much smaller than the size of the interaction region between the jet and the stellar wind. Thus, this problem can be reduced to that of a distributed source of mass that is injected into and thereafter advected with the jet flow. Bowman, Leahy & Komissarov (1996, hereafter BLK) studied the effect of mass loading by a typical stellar population on jets with different properties by solving the equations of evolution in steady state. In particular, they focused on light and hot electron/proton jets. They concluded that these jets can be efficiently decelerated by this mechanism, with some differences depending on the thermodynamical properties of the jets: hotter jets cool down due to entrainment of the cold wind particles, whereas relatively colder jets gain temperature in the entrainment region due to dissipation. Hubbard & Blackman (2006) studied the different ranges of stellar mass-loss rates and jet powers that could imply efficient jet deceleration within the host galaxy, and concluded that the stellar wind from a single Wolf-Rayet star could be enough to decelerate a weak FRI jet.

Laing & Bridle (2002b) constructed a one-dimensional model of the jet in 3C 31 using the basic conservation laws and the velocity field inferred by Laing & Bridle (2002a), which includes a substantial deceleration of the jet within the flaring region, located at 1–3 kpc from the central engine. Close to the outer boundary of this region, at 3.2 kpc, Laing & Bridle (2002b) found maxima in the mass entrainment rate (per unit length of the jet) both for their reference model and for the stellar mass input. However, the latter is much smaller. Although the expected mass injection by stellar winds seems to be enough to counterbalance the effects of adiabatic expansion and to keep the velocity fairly constant at the beginning of the flaring region, the continuous deceleration in the jet indicated by Laing & Bridle (2002a)’s results requires a monotonic increase of the entrainment rate at large distances. This cannot be the result of mass loss from stars, whose density falls rapidly with increasing radius. Laing & Bridle (2002b) concluded that entrainment from the galactic atmosphere across the boundary layer of the jet is the dominant mass input process far from the nucleus in this powerful ( $10^{44}$  erg s $^{-1}$ ) FRI jet, but that stellar mass loss might also contribute near the flaring point.

Laing & Bridle (2014) have recently presented observations and kinematic models for ten FRI radio galaxies. They concluded that the deceleration of FRI jets after the flaring point is a gradual process in which the transverse velocity profile evolves from constant to slower at the edges than on-axis. Mass loading by stars is distributed throughout the jet volume and is therefore not expected to create large transverse velocity gradients. It is therefore unlikely to be the dominant cause of deceleration on these scales: boundary-layer entrainment is more plausible. A contribution from stellar mass loading, particularly on smaller scales, is not excluded, however. This conclusion was based on models for the six sources with adequately determined transverse velocity profiles. It is consistent with, but not required by the models for the remaining four. All of the cases with well-

determined profiles are powerful FRI sources. It remains possible that weaker sources such as M84 and NGC193, for which the models do not show conclusive evidence for velocity gradients, are decelerated primarily by stellar mass loading.

In PM07 the deceleration and decollimation of the jet was produced by the development of a recollimation shock formed at a few kiloparsecs from the central engine due to the density decrease in the ambient IGM. The expansion caused by the jet overpressure as it propagated outwards and the subsequent recollimation shock effectively decelerated the jet after the shock, triggering the development of Kelvin-Helmholtz (KH) instabilities and enhancing the mass entrainment beyond this point. The main purposes of this paper are to extend the analysis of PM07 to include the combined effects of the mass loading of the jet by stellar winds and the recollimation shock, to compare with the earlier results and to cover a larger range of jet powers. We also investigate the effects of changing the boundary conditions of the simulations.

We present simulations of jets with typical FRI powers, including source terms in the equations of relativistic hydrodynamics that account for the mass entrainment by winds from the stellar populations expected for typical host galaxies. Our aim is to understand the conditions under which FRI jets can be decelerated by this type of entrainment and those for which either another process or a different stellar population are required.

The paper is structured as follows. The setup of the simulations, together with the parameters used are presented in Section 2, and the results are given in Section 3. Section 4 discusses the implications. A summary and the conclusions of this work are given in Section 5.

## 2 SIMULATIONS

### 2.1 Ambient medium and stellar mass-loss profile

In the simulations, the ambient medium is composed of a decreasing density atmosphere of ionized hydrogen in hydrostatic equilibrium. The profile for the number density of such a medium is (Hardcastle et al. 2002, PM07):

$$n_{\text{ext}} = n_0 \left[ 1 + \left( \frac{r}{r_c} \right)^2 \right]^{-3\beta_{\text{atm}}/2}, \quad (1)$$

with  $n_0 = 0.18$  cm $^{-3}$ ,  $r_c = 1.2$  kpc and  $\beta_{\text{atm}} = 0.73$ , where the contribution from the galaxy group atmosphere as used by PM07 is not included for simplicity.<sup>1</sup> This profile, in the simulated region (between 80 pc and 2 kpc), is plotted in Fig. 1. The temperature profile (Hardcastle et al. 2002, PM07) is close to constant with  $T_{\text{ext}} = 4.9 \times 10^6$  K over the simulated region. The external pressure is derived from the number density and temperature assuming pure ionized hydrogen (Hardcastle et al. 2002, PM07):

$$p_{\text{ext}} = \frac{k_B T_{\text{ext}}}{\mu X} n_{\text{ext}}, \quad (2)$$

<sup>1</sup> FRI radio sources are found in galaxies without group components: an example is NGC 315 (Croston et al. 2008).

where  $\mu = 0.5$  is the mass per particle in amu,  $X = 1$  is the abundance of hydrogen per mass unit, and  $k_B$  is Boltzmann's constant.

In addition to this external medium, we have included a law that accounts for mass entrainment into the jets from stellar winds, derived from a Nuker distribution of surface brightness in an elliptical galaxy (Lauer et al. 2007):

$$Q = Q_0 \left( \frac{r_b}{r} \right)^\gamma \left[ 1 + \left( \frac{r}{r_b} \right)^\alpha \right]^{(\gamma-\beta)/\alpha}, \quad (3)$$

where  $Q_0$  is the mass loss rate per unit area at  $r = 0$ ,  $r_b$  is the characteristic radius of the profile and  $\alpha$ ,  $\beta$  and  $\gamma$  are constants. The profile used in the simulations corresponds to the deprojection (Binney & Merrifield 1998) of the Nuker profile with  $r_b = 265$  pc,  $\alpha = 2.0$ ,  $\beta = 0.46$  and  $\gamma = 0.0$ , which fall well within the observed range (Lauer et al. 2007). This profile has been deprojected using a stellar distribution extending out to 20 kpc. The resulting mass-loss rate per unit volume in the simulated region is plotted against distance in Fig. 1. This profile results in an increasing total mass load per unit distance up to the end of the simulated grid. For other values of the parameters, the mass-loading rate can turn over within the 2 kpc simulation distance.

We parameterize the mass input by the central mass-loss rate per unit volume for the deprojected profile,  $q_0$ . We take  $q_0 = 4.95 \times 10^{22} \text{ g yr}^{-1} \text{ pc}^{-3}$  (a factor of ten smaller in the case of model D, see Table 1). For comparison, the central rate for the reference model of BLK is  $q_0 = 2.36 \times 10^{22} \text{ g yr}^{-1} \text{ pc}^{-3}$ . Our assumed profile gives a mass input rate per unit time and volume of  $5.9 \times 10^{21} \text{ g yr}^{-1} \text{ pc}^{-3}$  at 1.1 kpc (Fig. 1). At the same location (the starting point of their model), Laing & Bridle (2002b) find a very similar value of  $6.4 \times 10^{21} \text{ g yr}^{-1} \text{ pc}^{-3}$  (their Figs 1 and 11); that used by BLK in their reference model (their equation 12, Tables 1 and 2) is very slightly higher ( $7.2 \times 10^{21} \text{ g yr}^{-1} \text{ pc}^{-3}$ ). These differences are well within the uncertainties of the true mass input rate.

## 2.2 Jet parameters

Table 1 collects the parameters of the jets in our simulations. All of the simulated jets are purely leptonic and are injected at a distance from the galaxy nucleus of 80 pc with a radius  $R_j = 10$  pc. This assumes an opening angle of  $7^\circ$ , consistent with recent estimates of the opening angles of parsec-scale FRI jets (Müller et al. 2011; Asada & Nakamura 2012). The ambient density at injection is  $3 \times 10^{-25} \text{ g cm}^{-3}$ , and the ambient pressure is  $2.5 \times 10^{-10} \text{ erg cm}^{-3}$ .

We performed two simulations of jets with the same power as that in PM07, but including mass loading. Real jets are bipolar, but in order to save on computation time we have simulated only one side. This raises the question of the effect of the boundary conditions at injection. We have therefore made two simulations, identical except for the boundary conditions: *Powerful reflecting* (Pr), for a reflecting condition at the injection boundary of the numerical box, and *Powerful open* (Po), for an open boundary condition there. These simulations were designed to match as closely as possible the jet properties derived for 3C 31 (Laing & Bridle 2002a,b; Hardcastle et al. 2002), and the jets therefore have kinetic luminosities  $L_j = 10^{44} \text{ erg s}^{-1}$ , at the upper end of the power distribution for FRI sources.

Although models Po and Pr have the same jet power as that studied in PM07, they are simulated here for a shorter time ( $\simeq 0.25$  Myr instead of 7.3 Myr) and over a correspondingly shorter distance (2.2 kpc instead of 14.5 kpc). Mass-loading terms are included, however. In PM07, the injection of the jet into the numerical grid was done at 500 pc from the galactic nucleus, because the aim of the simulation was to study the long-term evolution. In this work, however, we are more interested in the influence of the mass loading of jets by stellar winds, so it is important to bring the injection point as close as possible to the centre of the galaxy, where the stellar density is highest. The initial cross-section must therefore be smaller (10 pc versus 60 pc in PM07). In order to keep the same injection power as in PM07, this difference in cross-section has to be compensated, resulting in an initially faster, denser and more overpressured jet here than in PM07. Models Po and Pr have jet Lorentz factor  $\simeq 7$  and jet to ambient density ratio  $3.2 \times 10^{-5}$  at injection. They are significantly faster, denser and colder than the other simulated jets we discuss below. They are also more overpressured with respect to the ambient.

The simulations of these models (to be discussed below) showed that the entrained mass is not high enough to decelerate the jets efficiently. We therefore ran a set of models (A, A0, B, C and D) with powers 200 times smaller. Reflecting boundary conditions were used in all cases. These model jets are relatively fast (Lorentz factor 3.2), light (jet to ambient density ratio  $10^{-8} - 10^{-10}$ ), hot (specific internal energy  $1.5 \times 10^2 - 1.5 \times 10^4 c^2$ ) and slightly underpressured with respect to the ambient (as a result of fixing the jet density and temperature). The one-dimensional estimate for the jet advance speed is  $4.3 \times 10^{-3} c$ . Model A0, exactly the same as model A but without any mass entrainment, serves as a reference to identify the effects of the mass entrainment on the jet collimation and propagation. The parameters of these models were selected to fall within the range used by BLK.

## 2.3 Computational setup

The two-dimensional grid reproduces the ambient medium of an elliptical galaxy in axisymmetric cylindrical coordinates. In the axial direction, the grid starts at 80 pc from the galactic centre and typically ends at 2 kpc, depending on the simulation. In the transversal direction, a homogeneous grid (with constant cell-size) covers up to 1 kpc, and is expanded by an extra grid with geometrically increasing cell size from 1 to 2 kpc. The jet is injected into the numerical grid (at 80 pc) with radius  $R_j = 10$  pc. The numerical resolution is 16 cells across the jet radius at injection. This translates into a homogeneous grid size of  $1600 \times 3200$  cells (transversal and axial, respectively).

For this work, we have modified the equations of conservation of mass, momentum and energy in order to account for mass loading from stellar winds and external gravity. The conservation equations for a relativistic flow in two-dimensional cylindrical coordinates ( $R, z$ ), assuming axisymmetry and using units in which  $c = 1$ , are:

$$\frac{\partial \mathbf{U}}{\partial t} + \frac{1}{R} \frac{\partial R \mathbf{F}^R}{\partial R} + \frac{\partial \mathbf{F}^z}{\partial z} = \mathbf{S}, \quad (4)$$

with the vector of unknowns

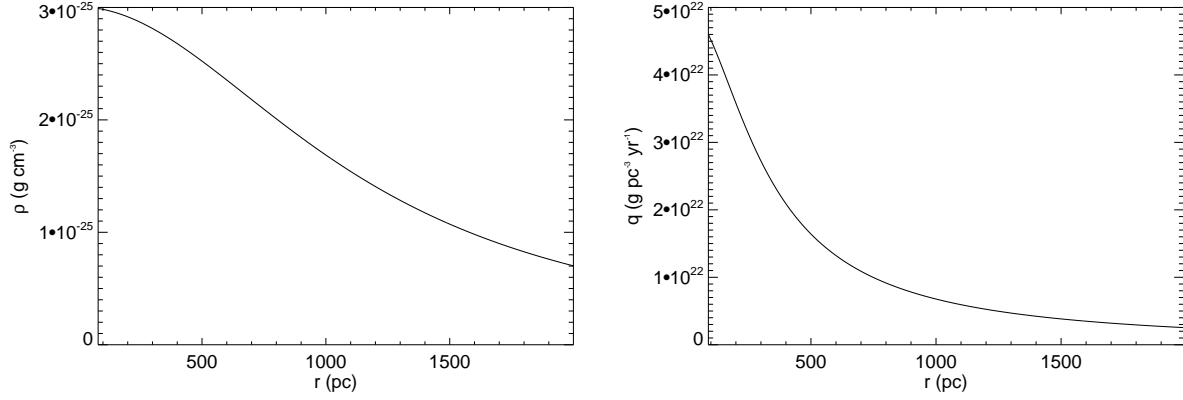


**Figure 1.** Radial profiles of ambient density (left panel) and stellar mass-loss rate per unit volume (right panel) in the simulated region for models Pr, Po, A, B and C. In the case of model D, the normalization factor for the mass-loss rate is smaller by one order of magnitude.

**Table 1.** Parameters of the simulated jets. (1) model name; (2) injection velocity (3) injection density; (4) jet temperature at injection; (5) jet to ambient pressure contrast at injection; (6) jet power; (7) central mass-entrainment rate; (8) jet length at the end of the simulation; (9) duration of the simulation.

Model	Velocity [c]	Density [g cm <sup>-3</sup> ]	Temperature [K]	$P_j/P_{\text{amb}}$	$L_j$ [erg s <sup>-1</sup> ]	$q_0$ [g yr <sup>-1</sup> pc <sup>-3</sup> ]	Jet length [kpc]	$t_{\text{sim}}$ [Myr]
Po	0.99	$9.65 \times 10^{-30}$	$3 \times 10^9$	17.6	$10^{44}$	$4.95 \times 10^{22}$	2.2	0.25
Pr	0.99	$9.65 \times 10^{-30}$	$3 \times 10^9$	17.6	$10^{44}$	$4.95 \times 10^{22}$	2.2	0.25
A0	0.95	$3 \times 10^{-33}$	$3 \times 10^{11}$	0.54	$5 \times 10^{41}$	0	1.5	1.6
A	0.95	$3 \times 10^{-33}$	$3 \times 10^{11}$	0.54	$5 \times 10^{41}$	$4.95 \times 10^{22}$	2.1	2.4
B	0.95	$3 \times 10^{-34}$	$3 \times 10^{12}$	0.54	$5 \times 10^{41}$	$4.95 \times 10^{22}$	2.0	2.1
C	0.95	$3 \times 10^{-35}$	$3 \times 10^{13}$	0.54	$5 \times 10^{41}$	$4.95 \times 10^{22}$	1.8	1.9
D	0.95	$3 \times 10^{-35}$	$3 \times 10^{13}$	0.54	$5 \times 10^{41}$	$4.95 \times 10^{21}$	1.8	1.8

$$\mathbf{U} = (D, D_1, S^R, S^z, \tau)^T, \quad (5)$$

fluxes

$$\mathbf{F}^R = (Dv^R, D_1v^R, S^Rv^R + p, S^zv^R, S^R - Dv^R)^T, \quad (6)$$

$$\mathbf{F}^z = (Dv^z, D_1v^z, S^Rv^z, S^zv^z + p, S^z - Dv^z)^T, \quad (7)$$

and source terms

$$\mathbf{S} = (qW_w, q_1W_w, qh_wW_w^2v_w^R + p/R + g^R, qh_wW_w^2v_w^z + g^z, qW_w(h_wW_w - 1) + v^Rg^R + v^zg^z)^T. \quad (8)$$

The five unknowns  $D, D_1, S^R, S^z$  and  $\tau$ , refer to the densities of five conserved quantities, namely the total and leptonic rest masses, the radial and axial components of the momentum, and the energy (excluding the rest mass energy). All five unknowns are defined in the laboratory frame, and are related to the quantities in the local rest frame of the fluid (primitive variables) according to:

$$D = \rho W, \quad (9)$$

$$D_1 = \rho_1 W, \quad (10)$$

$$S^{R,z} = \rho h W^2 v^{R,z}, \quad (11)$$

$$\tau = \rho h W^2 - p - D, \quad (12)$$

where  $\rho$  and  $\rho_1$  are the total and the leptonic rest-mass densities, respectively,  $v^{R,z}$  are the components of the velocity

of the fluid.  $W$  is the Lorentz factor [ $W = (1 - v^i v_i)^{-1/2}$ , where summation over repeated indices is implied], and  $h$  is the specific enthalpy defined as

$$h = 1 + \varepsilon + p/\rho, \quad (13)$$

where  $\varepsilon$  is the specific internal energy and  $p$  is the pressure. Quantities  $g^R$  and  $g^z$  in the definition of the source-term vector  $\mathbf{S}$ , are the components of an external gravity force that keeps the atmosphere in equilibrium.

The difference between these equations and those used in PM07 is just the inclusion of the source term related to mass loading by stellar winds. In the source-term vector, the subscript w refers to the stellar wind and  $q$  represents the mass-loading rate per unit volume defined by deprojecting the expression in equation (3), as plotted in Fig. 1. The wind is taken to be a cold electron-proton gas entrained with negligible velocity compared to the jet. Thus we neglect the terms depending on the internal energy and temperature and take  $h_w = 1$ ,  $v_w^R = v_w^z = 0$ ,  $W_w = 1$ , so

$$\mathbf{S} = (q, q_1, p/R + g^R, g^z, v^R g^R + v^z g^z)^T, \quad (14)$$

with  $q_1 = q m_e / m_p$ . The system is closed by means of the Synge equation of state (Synge 1957), as described in Appendix A of PM07. This accounts for a mixture of relativistic Boltzmann gases (in our case, electrons, positrons and protons). The code also integrates an equation for the jet mass

fraction,  $f$ . This quantity, set to 1 for the injected jet material and 0 otherwise, is used as a tracer of the jet material through the grid.

The simulations presented in this paper use the finite-volume code *Ratpenat*. This is a hybrid – MPI + OpenMP – parallel code that solves the equations of relativistic hydrodynamics in conservative form using high-resolution-shock-capturing methods (see Perucho et al. 2010, and references therein): (i) primitive variables within numerical cells are reconstructed using PPM routines; (ii) numerical fluxes across cell interfaces are computed using the Marquina flux formula and (iii) advance in time is performed with third order TVD-preserving Runge-Kutta methods.

The evolution of the jets in simulations A, B, C and D has been followed up to 1 – 2 Myr (see Table 1), by which time the jets have propagated between 1 and 2 kpc. This is far enough to capture the effect of mass loading on jet flaring and disruption. Each simulation needed about 4 million time steps.

Simulations A, B, C and D were performed in Magerit, at the Supercomputing and Visualization Center of Madrid, within the *Red Española de Supercomputación* (Spanish Supercomputing Network), with up to 48 processors. Processors were added as the jet evolved (starting with 8 processors). These simulations required between  $1.0 \times 10^5$  and  $1.5 \times 10^5$  computational hours, depending on the model, resulting in a total of around  $5 \times 10^5$  hours.

### 3 RESULTS

#### 3.1 The influence of boundary conditions on jet evolution

We first describe the effects resulting from the change of boundary conditions from open (as used in PM07) to reflecting. Reflecting boundary conditions mimic the presence of a counter-jet with the same properties as the simulated jet and are therefore likely to be more realistic. Fig. 2 shows the last frames of both simulations at  $t \simeq 2.5 \times 10^5$  yr. The images reveal the main differences due to the boundary condition: the shape of the bow-shock (the forward shock driven into the ambient by the injection of the jet), the width of the jet and the prominence of jet pinching. In Pr, the reflecting boundary condition causes both the bow-shock and the inner cocoon (the region with mixed shocked ambient and jet material surrounding the jet) to be wider. The jet in Po is broader and shows stronger recollimation (conical) shocks, which in turn make the head of the jet broader. The jet in Pr remains more collimated.

The choice of boundary condition only affects some aspects of the simulations. For example, the advance speeds of the jet terminal shock and the head of the bow-shock are very similar in Pr and Po, whereas the cocoon pressure and density in Pr are larger: by almost an order of magnitude in the density ( $\sim 1.5 \times 10^{-26}$  compared with  $\sim 2 \times 10^{-27}$  g cm $^{-3}$ ) and a factor of two in the pressure ( $\sim 4 \times 10^{-9}$  compared with  $\sim 2 \times 10^{-9}$  erg cm $^{-3}$ ) by the end of the simulations. The pressure is basically determined by the injected energy divided by the volume of the shocked region, implying that the pressure in the shocked ambient and jet material (i.e. the whole volume within the bow-shock, excluding the jet) will decrease with time as it expands. The

pressure in the cocoon follows the same power-law  $P_c \propto t^{-0.9}$  in both cases, but with a larger constant of proportionality for Pr. The radius of the bow-shock also increases faster with time for Pr: by the end of the simulation the mean radius of the shocked region is  $\simeq 500$  pc compared with  $\simeq 400$  pc in Po. Another consequence of the higher pressure in Pr is that the opening angle of the jet is smaller ( $\simeq 0^\circ.27$  versus  $\simeq 1^\circ.1$  in Po). The recollimation shocks are therefore stronger in Po.

Po also shows a broader and faster backflow component than Pr, since backflowing material can escape through the open boundary. In both simulations, the backflow decelerates with the distance travelled from the terminal shock. Typical velocities close to the terminal shock ( $z \simeq 2$  kpc) are similar in both cases:  $\simeq 0.6c$  in Pr and  $\simeq 0.7c$  in Po. In Pr, the velocity drops to values  $\simeq 0.4c$  at  $z \simeq 1.5$  kpc and  $\simeq 0.2c$  at  $z \simeq 1$  kpc, finally reaching zero at  $z = 80$  pc, close to the reflecting boundary. In Po, the backflow velocity is typically  $\simeq 0.5c$  at  $z \simeq 1$  kpc and drops to values  $\simeq 0.2c$  at  $z = 80$  pc.

As the jet in both simulations has the same injection conditions, we expect that the jet and shock structures seen in Pr and Po should be very similar if they are compared at the same cocoon pressure. In other words, Pr at a given time will look quite similar to Po seen at some earlier time. In particular, the pressure in the cocoon has a direct influence on the position of a possible recollimation shock, and the appearance of strong shocks in simulations with reflecting boundaries will occur at later times than in simulations with open boundaries. We thus conclude that the shock in the jet in PM07 (which used an open boundary) would correspond to an older jet simulated with a reflecting boundary condition, in which the bow shock would have propagated to larger distances than the 15 kpc found in that work.

As the use of a reflecting boundary condition is likely to give a better approximation to the true bipolar case, we use it for the remaining simulations in this paper. The differences introduced by the change of boundary conditions should be borne in mind when comparing with the simulations of PM07.

#### 3.2 Mass loading of powerful jets

##### 3.2.1 Absence of deceleration by mass loading

Neither of the simulations of powerful, mass-loaded jets show signs of strong deceleration over distances of 2 kpc, but there is slow deceleration due to a combination of mass loading and dissipation of kinetic energy at internal shocks. The jet flow heats up at the shocks, increasing its temperature by an order of magnitude (to  $\sim 3 \times 10^{10}$  K) between injection and the terminal shock. The role of mass loading is revealed by a decrease in the jet mass fraction from 1 to around 0.9 on the axis (slightly larger for Pr and smaller for Po) and a decrease in the mean value over the jet cross section to about 0.6 before the jet terminal shock in both simulations. The mean jet flow velocity before the terminal shock is around 80% of the injection value.

The jet can only be slowed efficiently by mass loading when the kinetic energy required to accelerate the loaded mass to the flow velocity of the jet ( $W_j \dot{M} c^2$  per unit time, where  $W_j$  is the jet Lorentz factor, and  $\dot{M}$  is the mass-

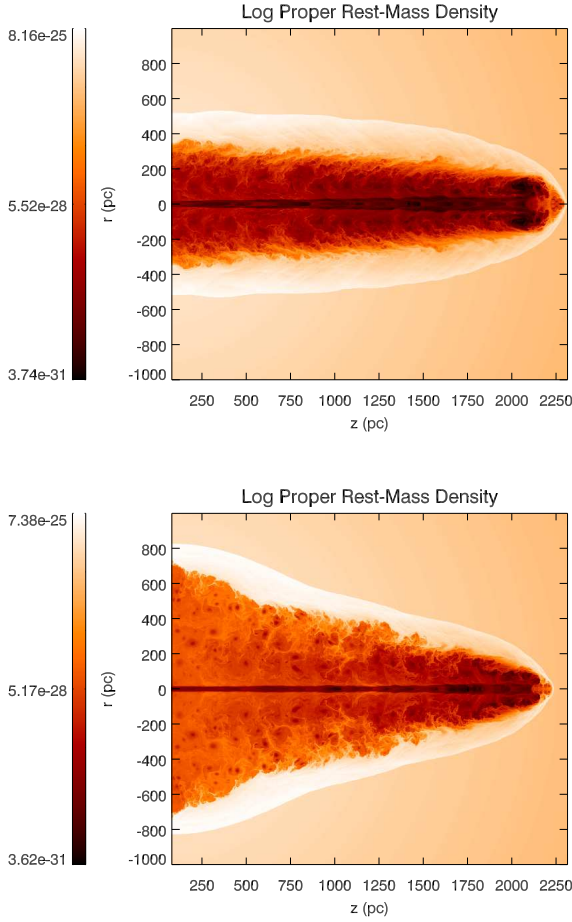


**Figure 2.** Maps of the logarithm of the rest-mass density at the end time ( $t \simeq 2.5 \times 10^5$  yr) for simulations Po (upper panel) and Pr (lower panel).

loading rate) is of the order or larger than the kinetic luminosity,  $L_j$  (Hubbard & Blackman 2006). If we assume a constant mass-loading rate per unit volume  $q$  and a jet of constant radius  $R_j$ , the characteristic length for jet deceleration is

$$l_d \simeq \frac{1}{W_j} \left( \frac{L_j}{10^{44} \text{ erg s}^{-1}} \right) \left( \frac{q}{10^{22} \text{ g yr}^{-1} \text{ pc}^{-3}} \right)^{-1} \left( \frac{R_j}{10 \text{ pc}} \right)^{-2} \text{ Mpc.} \quad (15)$$

Even if we use a constant mass-loading rate equal to the maximum at the centre of the galaxy,  $q = q_0 = 4.95 \times 10^{22} \text{ g yr}^{-1} \text{ pc}^{-3}$  (Table 1), we still obtain deceleration lengths of the order of hundreds of kpc. Such values are only indicative, since: (i) part of the jet kinetic energy will be used to heat the loaded material; (ii) the mass loaded per unit time rises as the jet gets longer and (iii) the true value of the mass-loading rate per unit volume decreases very fast with increasing distance from the galaxy centre (for  $r \gtrsim r_b$  in our models), so the approximation  $q \approx q_0$  is only valid over distances  $\lesssim 1$  kpc. Whereas (i) and (ii) tend to decrease the deceleration length, (iii) tends to increase it. Nevertheless, this simple computation clearly explains the lack of deceleration in models Po and Pr within the first 2 kpc.

### 3.2.2 Comparison between models with and without mass loading

It is interesting to compare Po and Pr with the simulation presented in PM07 (which has the same boundary condition as Po). Note that the flow parameters at injection are quite different, even though the jet power is the same in all three cases. In PM07, the jet was injected at 500 pc, with a radius of 60 pc, a velocity  $v_j = 0.87 c$  and an overpressure factor of 7.8 with respect to the ambient value. The jets in Po and Pr were injected at 80 pc, with a radius of 10 pc, a velocity  $v_j = 0.99 c$  and an overpressure factor of 17.6.

In PM07, the first recollimation shock appeared at  $z \simeq 1$  kpc after  $t \simeq 8 \times 10^5$  yr. The jet was injected close to the core radius of the galactic gas, and thus expanded into an ambient medium in which the density and pressure fall rapidly with distance. Within this environment the pressure of the cocoon evolves as  $P_c \propto t^{-1.3}$ . In the case of Po and Pr, the simulations covered much smaller durations ( $t \simeq 2.5 \times 10^5$  yr) and distances from the nucleus than that in PM07. The cocoon pressure evolves following a flatter slope  $P_c \propto t^{-0.9}$ , primarily because the jets in Po and Pr are entirely within the galactic core, where the ambient density falls very slowly with distance. This results in a slower expansion: the jets in Po and Pr would need to be followed to larger distances and times to be directly compared with the simulation in PM07.

## 3.3 Mass loading of weak jets

### 3.3.1 Reference model without mass loading

Fig. 3 displays a series of snapshots of the rest mass density of model A0, in which there is no mass loading. The sequence shows the propagation of the shock generated by the jet through the ambient. The weakness of the jet is reflected in the almost spherical shape of this shock at very early times (Fig. 3, first panel), the low Mach number of the jet ( $\approx 3$  at the beginning of the simulation) and the clear detachment of the shock from the cocoon. The contact discontinuity between the cocoon and the shocked ambient soon develops a prominent ‘nose-cone’ and the bow-shock becomes more extended in the axial direction. The beam<sup>2</sup> shows a series of internal conical shocks produced by the pressure mismatch between it and the cocoon.

Fig. 4 shows the distributions of pressure, rest-mass density, temperature and axial flow velocity at the end of the simulation. The protrusion of the bow shock caused by the impact of the beam on the originally spherical shock is clearly seen in the first three panels. Conical shocks within the beam are apparent in the pressure, rest-mass density and axial velocity panels. These eventually evolve into planar disrupting shocks. The supersonic beam ends at a terminal shock where the beam flow decelerates, compresses and heats. In Fig. 4, this shock is located at about 1 kpc from the injection point. The region between this shock and the bow shock forms the so-called head of the jet, a very dynamic

<sup>2</sup> In the following, we will refer to the whole outflow structure (observed or simulated) as the *jet*, and to the fast and collimated central spine of the (simulated) jet as the *beam* in order to clarify the presentation of the results.

structure that governs the propagation of the jet through the ambient. In model A0, the region is quite broad with no substantial enhancement of the internal energy density (Fig. 4; pressure panel); the terminal shock, and hence the jet, are still propagating at the end of the simulation, and have not stalled. The dynamics of the jet head is discussed in more detail in Section 4.4. The cocoon is essentially isobaric, since the time-scale for the pressure to become constant is much shorter than the propagation time-scale. The density and temperature distributions display a clear transition between the almost homogeneous values of the old jet material in the cocoon (made colder and denser due to mixing with the shocked ambient gas through the contact discontinuity) and the hot and dilute material newly injected at the nose cone. Finally, a hot shear layer develops between the beam and cocoon material (this is not seen in the temperature panel of Fig. 4 due to its limited resolution).

We emphasize that the end-points of all of the simulations presented here correspond to very early stages of the evolution of low-power radio galaxies. This is the main reason why the nearly spherical region of gas surrounding the base of the jet in model A0 ( $\approx 700$  pc in radius in Fig. 4) appears much hotter and less dense than the cool cores revealed by X-ray observations in the host galaxies of FR I sources (Hardcastle et al. 2002; Croston et al. 2008), and indeed included in the initial conditions for the simulations. The hot cocoons will dilute and mix with the cooler ambient material as the jet becomes transonic and the bow shock disappears. The spherical shape that we find for the cocoon close to the injection is due to the low advance velocity of the head of the jet and the action of gravity: the dynamical time-scale of the gravitational field that maintains the atmosphere in hydrostatic equilibrium is in the range  $t_D \simeq 10^5$  yr to  $\simeq 3 \times 10^5$  yr in the simulated region; this is smaller than the simulation time<sup>3</sup>.

### 3.3.2 Weak jet models with mass loading: Model A

Figs 5 and 6 are the equivalents for model A of Figs 3 and 4 for model A0. The times of the snapshots in Figs 3 and 5 are almost identical, allowing a direct comparison of the density panels for the two models. The main structural and dynamical features of the cocoon/shocked ambient system found in model A0 (an almost spherical cocoon, detachment of the bow shock from the cocoon and formation of a nose cone at the head of the jet) also apply to model A. Comparison between the two sequences also shows very similar speeds for the propagation of the jet head and the expansion of the cocoon. These similarities persist until the ends of the simulations (Figs 4 and 6). The reasons for them are discussed in Section 4.2.

However, qualitative differences in the evolution of A0 and A appear as a result of the accumulated effect of mass loading. In particular, the mass loading causes an efficient deceleration of the plasma within the beam in model A,

which leads to expansion. The increase of the beam cross section reduces the momentum transfer per unit area to the ambient and causes the jet to decelerate. As a result, the beam in model A is denser, cooler and shorter than the one in model A0 and expands with an almost constant half-opening angle of  $\approx 1.5^\circ$  until its disruption at about 900 pc from the nucleus (Fig. 6). Whereas the beam in model A0 propagates at almost constant speed, the terminal shock in model A decelerates with time and nearly stalls by the end of the simulation (see Section 4.4). Mass loading and the accompanying jet expansion appear to reduce pinching along the jet in model A relative to model A0, so the conical shocks are weaker in the former case (compare the pressure panels of Figs 3 and 5). However, pinching is more disruptive at the jet head in model A and is the main cause of the flaring.

### 3.3.3 Weak jet models with mass loading: Models B and C

Models A, B and C (see Table 1) form a sequence along which the density at injection decreases by a factor of one hundred and the specific internal energy increases by the same amount, keeping the same power (and thrust) for the jets. We do not show the early evolution of models B and C (very similar to that of model A), and concentrate on the distributions of pressure, rest-mass density, temperature and axial flow velocity at the end of simulation C (Fig. 7), which show the largest differences compared with A. The differences in the overall structure of the jet/cocoon/shocked ambient system between models A (Fig. 6) and C are very small (Section 4.2). The similarity between these two models extends to the beam structure, with very similar distributions of density, pressure and flow velocity. The obvious conclusion (analysed in detail in Section 4.3) is that the dynamics of the beams in models A, B and C are dominated by the process of mass loading with the thermodynamical properties playing a secondary role.

### 3.3.4 Weak jet models with low mass loading: Model D

Model D has the same jet injection conditions as model C but a central mass-loading rate per unit volume,  $q_0$ , one order of magnitude smaller (Table 1). Fig. 8 shows the distributions of pressure, rest-mass density, temperature and axial flow velocity of model D at the end of the simulation. The gross morphology of the jet/cocoon/shocked ambient ensemble is again almost identical to that of models A, B and C (and A0), as explained in Sect. 3.3.2. In spite of two orders of magnitude difference in the beam density (and temperature), model D resembles model A0 more than models A and C: the beam remains fast and well-collimated, with strong conical shocks. This result proves again the sensitivity of the beam structure and dynamics to the mass loading rate and the secondary role of the jet thermodynamics, within the range of parameters used in these simulations.

<sup>3</sup> These numbers have been obtained using the dark-matter density profile that are needed to keep the atmosphere of gas in hydrostatic equilibrium and estimating  $t_D \sim (G \rho_{DM})^{-1/2}$ , where  $G$  is the gravitational constant and  $\rho_{DM}$  is the density of dark matter within the simulated region.

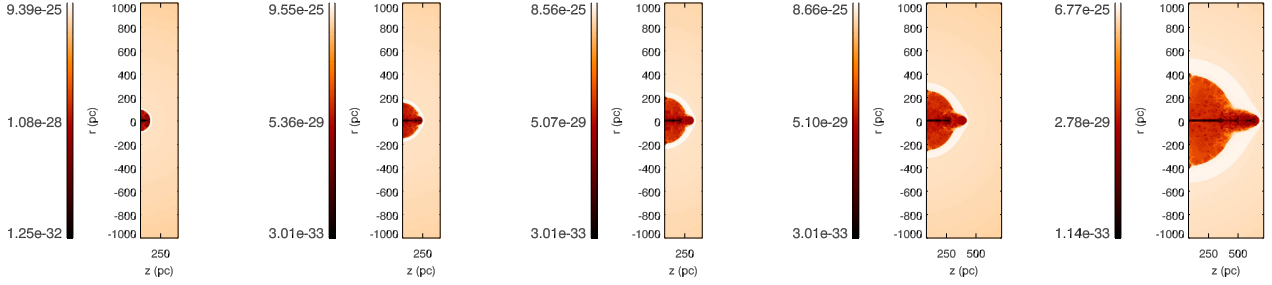


**Figure 3.** Evolution of the rest-mass density distribution in model A0. From left to right, the times of the frames are  $6.5 \times 10^4$ ,  $1.3 \times 10^5$ ,  $1.9 \times 10^5$ ,  $2.9 \times 10^5$ ,  $5.8 \times 10^5$  yr.

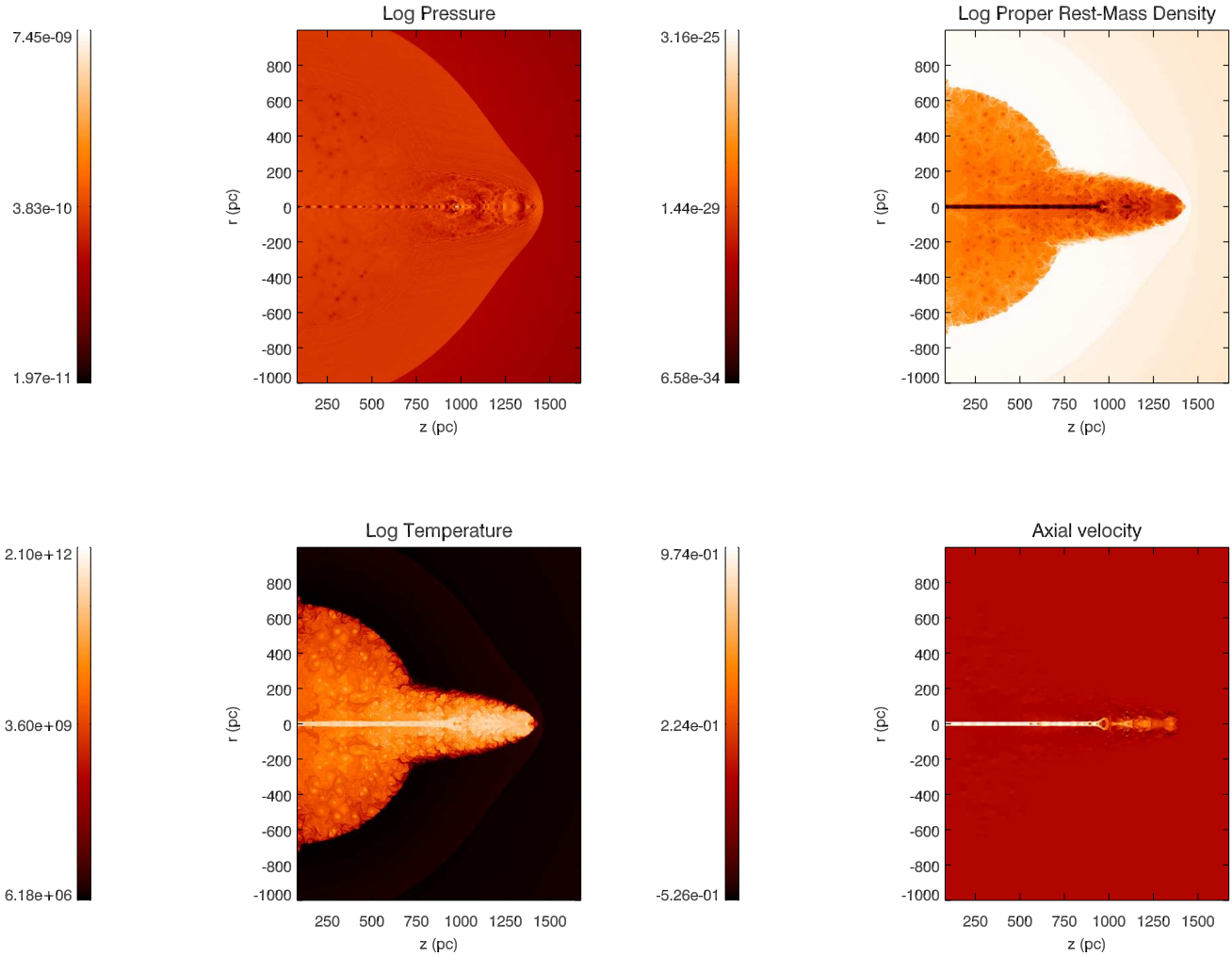


**Figure 4.** Pressure, rest-mass density, temperature and axial flow velocity in model A0 at the end of the simulation ( $t = 1.6 \times 10^6$  yr).

## 4 DISCUSSION

### 4.1 Comparison with previous work on stellar mass loading

The parameters defining the ambient medium, the mass-loss rates and the jets in models A, B, C and D are similar to those in BLK, allowing a comparison between the two sets of

simulations. In particular, the central mass-loss rate of the two reference models in BLK ( $2.36 \times 10^{22} \text{ g yr}^{-1} \text{ pc}^{-3}$ ) lies between those for models A, B and C ( $4.95 \times 10^{22} \text{ g yr}^{-1} \text{ pc}^{-3}$ ), and model D ( $4.95 \times 10^{21} \text{ g yr}^{-1} \text{ pc}^{-3}$ ). The kinetic luminosity per unit area at injection of our models is about four times smaller than that of the cold reference model in BLK, and just a bit larger than that of their hot model. Finally,



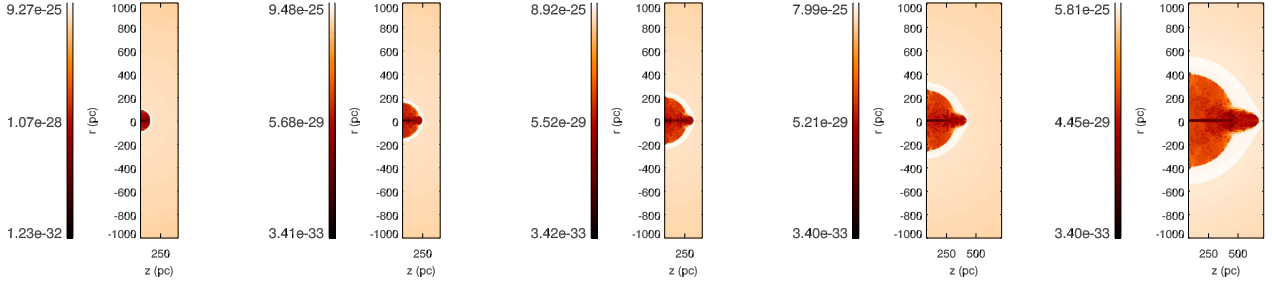


**Figure 5.** Evolution of the rest-mass density distribution in model A. From left to right, the times of the frames are  $6.5 \times 10^4$ ,  $1.3 \times 10^5$ ,  $1.9 \times 10^5$ ,  $2.9 \times 10^5$ ,  $6.0 \times 10^5$  yr.

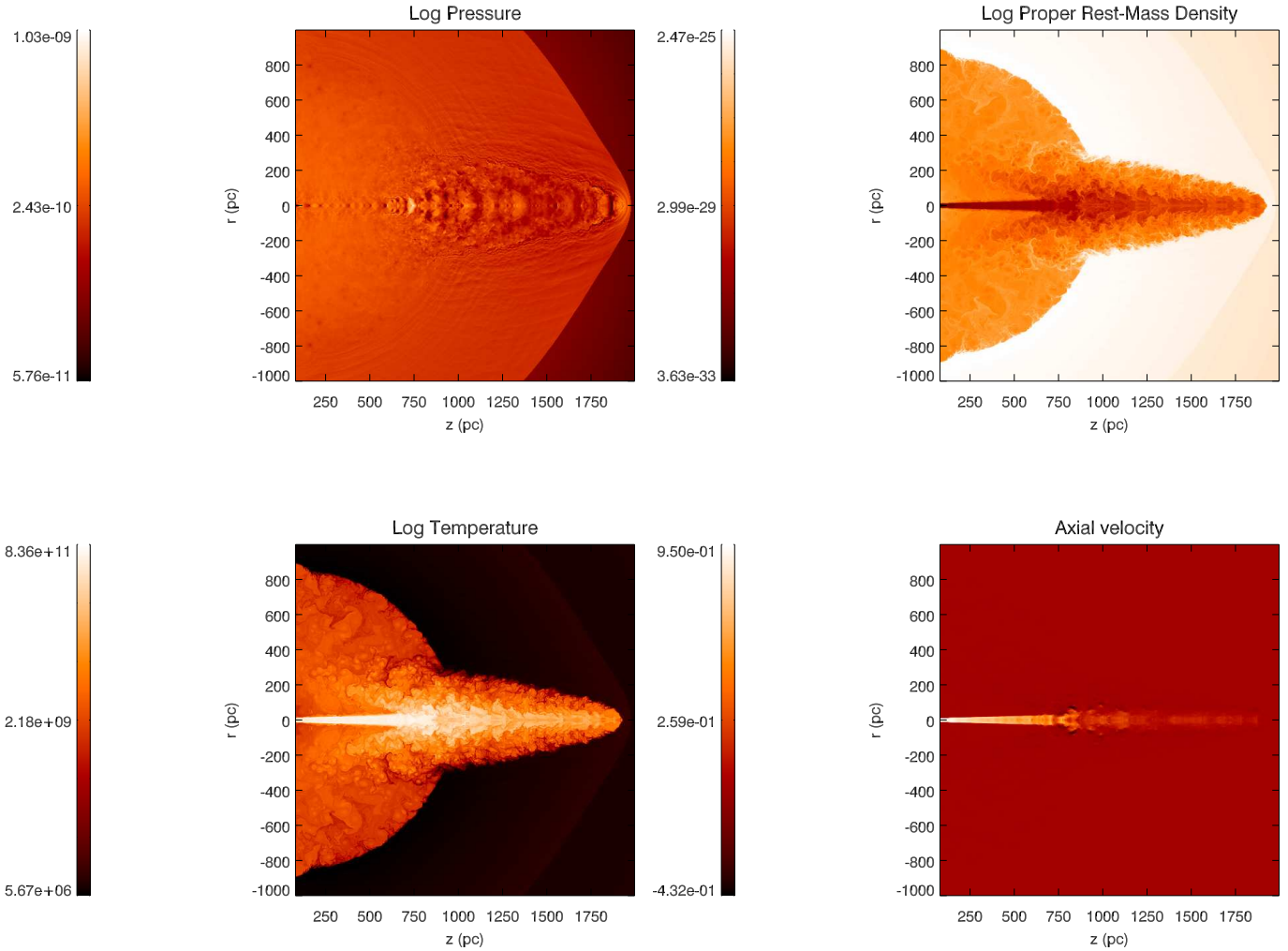


**Figure 6.** Pressure, rest-mass density, temperature and axial flow velocity in model A at the end of the simulation ( $t = 2.4 \times 10^6$  yr).

the Lorentz factor of the flow at injection is 3 in models A, B, C and D, and 5 in BLK's reference models. The deceleration lengths,  $l_d$ , predicted by equation (15) are therefore in the ratios:  $l_{d,A,B,C} : l_{d,hot} : l_{d,cold} : l_{d,D} \approx 1 : 1 : 4.5 : 10$ . This prediction is in qualitative agreement with our results and those of BLK. Our models A, B and C all show deceleration, as do the hot and cold reference models of BLK, with

the former having a shorter stopping distance (their Figs 3 and 4). Model D, by comparison, shows little deceleration.

The bulk parameters governing the propagation of the jets in our simulations are similar to those of BLK, but differences are expected from the disparity in the composition and thermodynamic properties between the models and from the natures of the two kinds of simulation. Our

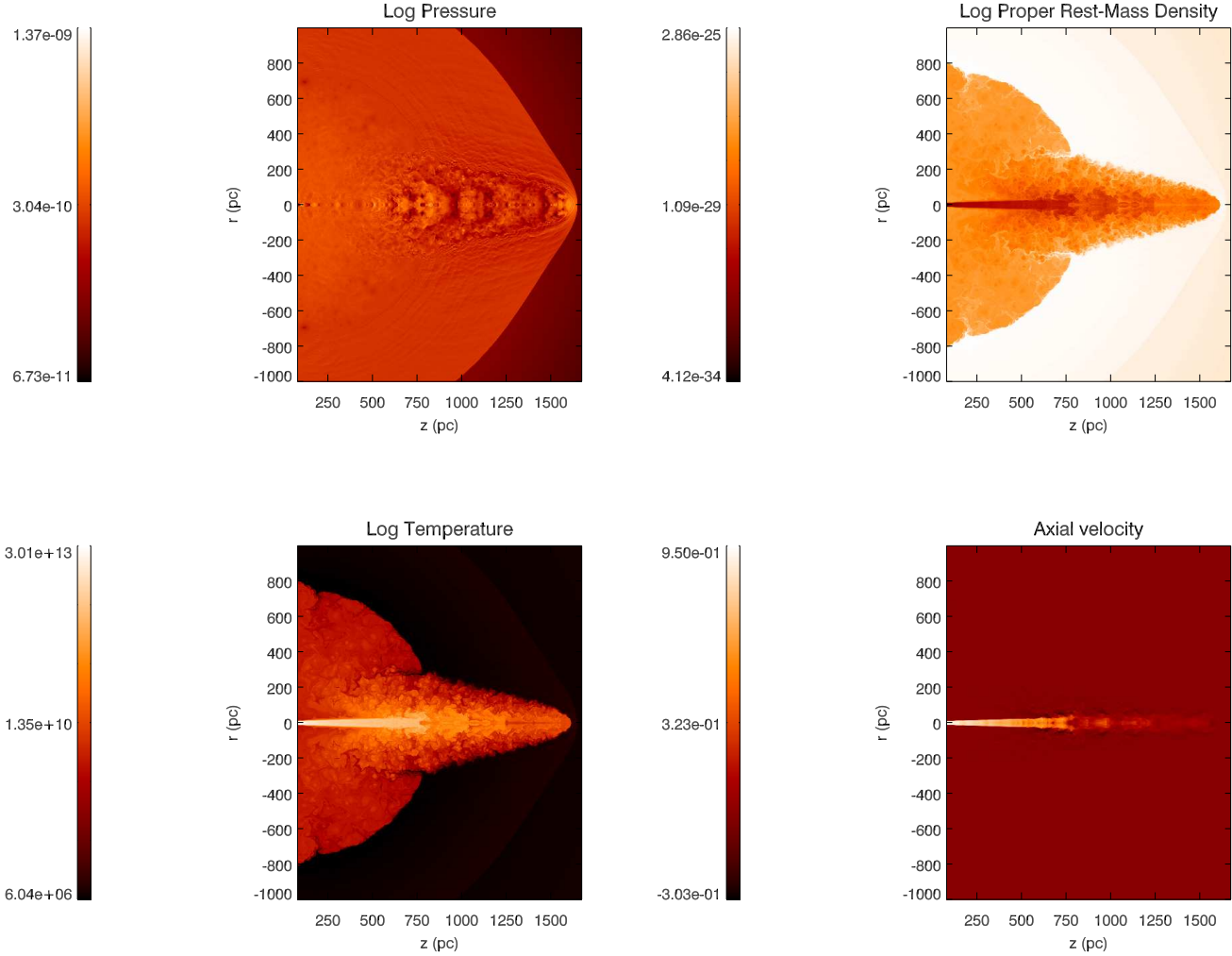


**Figure 7.** Pressure, rest-mass density, temperature and axial flow velocity in model C at the end of the simulation ( $t = 1.9 \times 10^6$  yr).

jets are composed of electron-positron pairs; those of BLK contain electron-proton plasma. Thus, although the temperatures of the two sets of models cover the same range ( $\approx 3 \times 10^{11} - 3 \times 10^{13}$  K), all of our models are thermodynamically hot. The simulations in BLK assume steady flows. They are therefore best suited to describe a long, isolated jet propagating through a prescribed (and undisturbed) ambient medium. Our simulations are dynamical and allow us to study the complex head of the jet, the formation of a cocoon and the process of flaring and disruption. They are, however, restricted to the early evolutionary phases of FRI radio sources.

#### 4.2 Evolution of the cocoon and shocked ambient gas

The gross morphological and dynamical properties of the shocked ambient and cocoon in models A, B, C, D and A0 are all very similar. The explanation is that all of the models have the same kinetic power and thrust ( $\approx L_j/c = 1.7 \times 10^{31}$

dyn) and propagate through the same ambient medium, so the differences between their gross dynamical properties are small. Fig. 9 shows the evolution of the length and width of the shocked region with time for all of the models. The differences among the models are tiny, particularly for the sideways expansion. The axial expansions fall in two groups (although with a difference in expansion speed of only a few percent), with models A0 and D (not affected by the mass loading) undergoing the faster expansion. In models A, B and C, second-order effects related to the mass loading of the jet slow the expansion slightly (e.g. the increase in the jet cross section reduces the jet thrust per unit area).

#### 4.3 Beam structure

Although limited in duration, our simulations allow us to study the principal effects of mass loading on the beam evolution because the jet head is followed out to a distance of  $1 - 2$  kpc, well beyond the stellar break radius  $r_b = 260$  pc.

The internal structure of the jets is dominated by

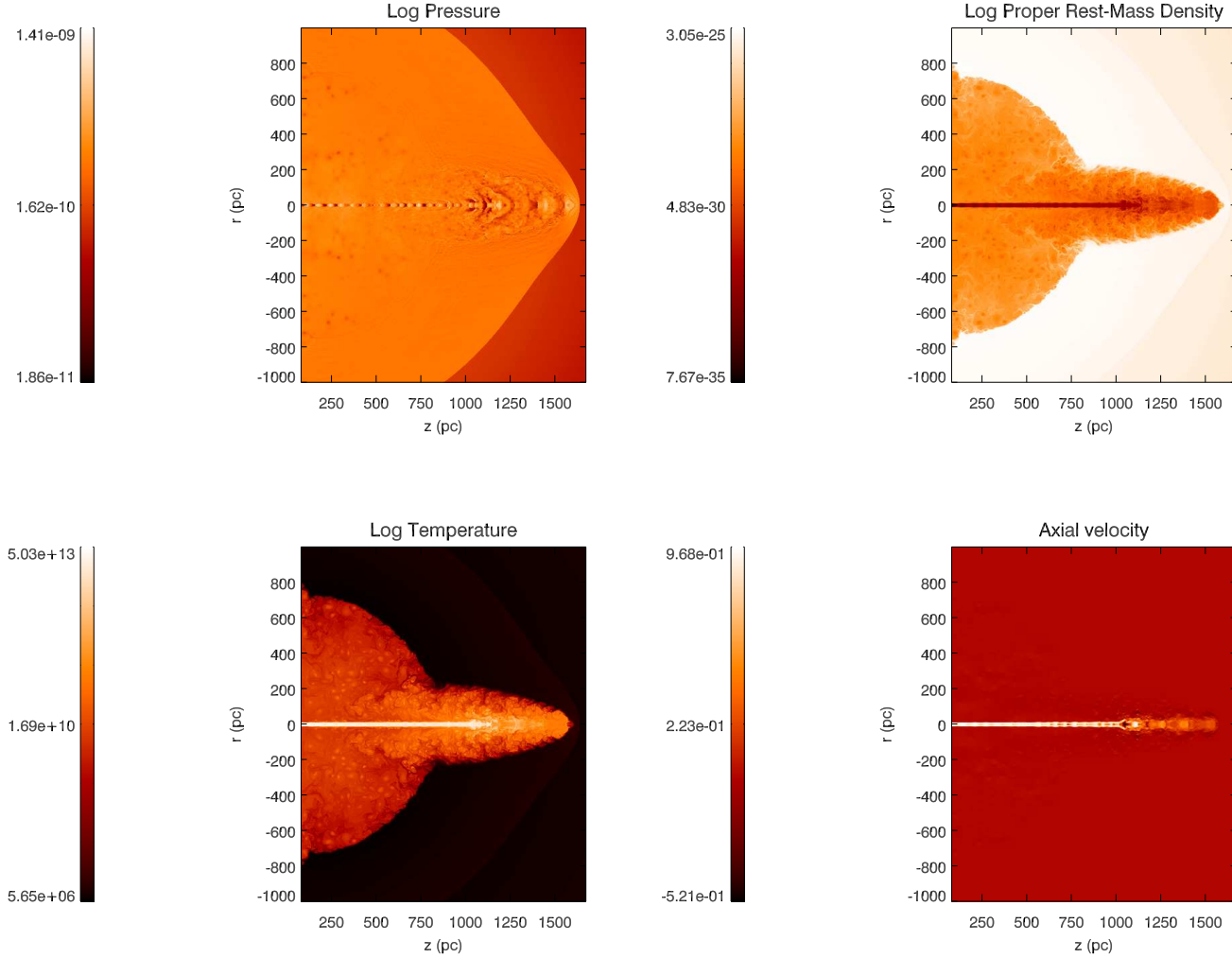


**Figure 8.** Pressure, rest-mass density, temperature and axial flow velocity in model D at the end of the simulation ( $t = 1.8 \times 10^6$  yr).

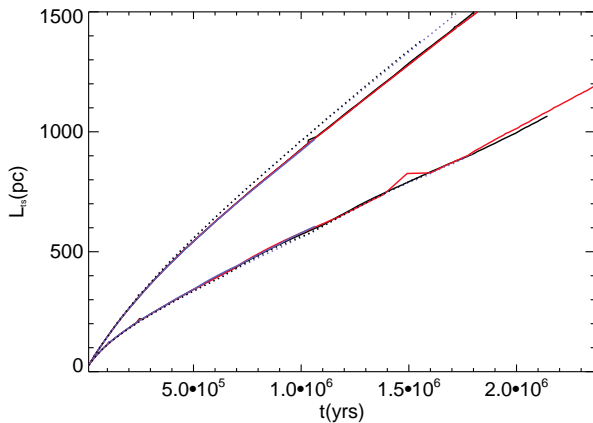


**Figure 9.** Length (top set of lines) and width (bottom set) of the shocked region as functions of time for models A, B, C, D and A0. Filled black: A; filled red: B; filled blue: C. Dotted black: A0; dotted blue: D.

oblique shocks (conical shocks in axisymmetric models). Their origin is the pressure mismatch between the beam and its surroundings (i.e., the cocoon) and this produces periodic variations of the beam structure around some state of equilibrium. The wavelength of these variations is given approximately by  $\mathcal{M}R$ , where  $\mathcal{M}$  is the relativistic Mach number and  $R$  is the beam radius (Wilson 1987). At the incident shock, the beam flow recollimates and decelerates whereas at the reflected shock, the flow is first compressed and then expands and accelerates, helped by the pressure gradient in the post-shock gas. The expansion continues until the pressure drops below the ambient value, when a new incident shock is initiated. Fig. 10 shows a sketch of a conical shock. If the initial jet overpressure is large or the fall in the ambient pressure is steep enough, the shock can produce a planar Mach disk, as observed in PM07. The series of oblique shocks left behind by the jet head is present in all of the models but is especially prominent in models A0 (Fig. 4) and D (Fig. 8). It is apparently unaffected by the small amount of mass loading in the latter case. In the more heavily mass loaded models A, B and C, the internal shocks

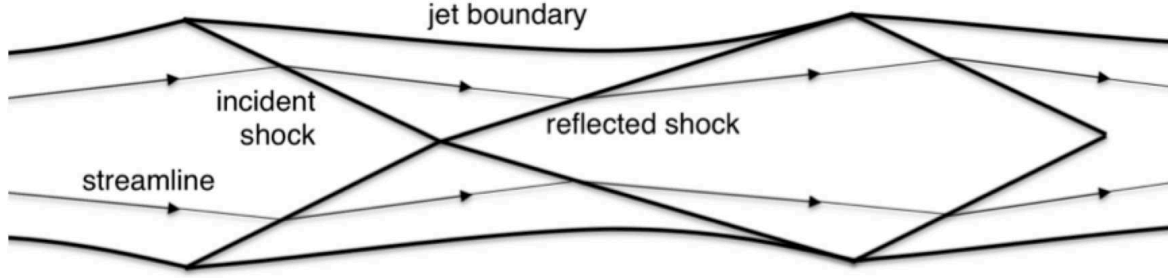


**Figure 10.** Sketch of the generation of a conical shock in a supersonic jet. For small pressure differences, the shocks are conical. If the initial jet overpressure is large or the fall in the ambient pressure is steep enough, the shock can produce a planar Mach disk, as observed in PM07.

are weaker (and the amplitudes of the pressure jumps are therefore smaller than in models A0 or D).

A simple analysis of the beam properties can be done by assuming stationarity from the injection point to the terminal shock. This is a fair assumption as long as the beam remains supersonic (which is certainly the case up to the terminal shock) and the injection boundary conditions and the mass loading are also stationary. The external pressure around the jet (the cocoon pressure) is quite homogeneous and varies slowly with time. The evolution of the averages across the beam of different relevant quantities along the axial direction can then be evaluated. To this end, the beam is defined as the domain encompassing all of the plasma with axial velocity larger than  $0.4c$ . The radius of this region is plotted against axial distance,  $z$ , in Fig. 11(a). The value of  $0.4c$  represents a compromise that gives a well-defined beam profile up to the terminal shock at the cost of including a fraction of cocoon material accelerated by shear at the beam/cocoon surface in the analysis. As noted in Section 3.3.3, the beam profiles are remarkably similar for models A, B and C. This is primarily a consequence of mass loading dominating the beam structure, with the detailed thermodynamics of the different beam models playing a secondary role. The beam radius profile in model D remains close to that of model A0 and this confirms that the mass-load rate in model D is not strongly affecting the dynamics of the jet.

The primary effect of mass loading on the beam is the deceleration and cooling of the flow as a result of the momentum transfer from the original beam fluid to the newly incorporated material and the reduction of the mean specific internal energy. Figs 11(b) and (c) show, respectively, the averages of the flow velocity and the specific internal energy across the beam as functions of axial distance for models A, A0, B, C and D at the end of the simulations. The deceleration of the beam flow in models A, B and C is clear. Despite the differences in initial specific internal energy and density (two orders of magnitude between the extreme cases), the deceleration rate in these models is roughly the same. This is because these initial values have been chosen so that all three models have the same initial internal energy per unit volume and the same thrust (Table 1). The density profiles are dominated by stellar mass input (except very close to the injection point) and are also very similar (Fig. 11e). The deceleration rate depends on the initial momentum of

the beam and the mass-loading rate, which are both the same in all three models. Similarly, the models all have the same amount of internal energy to share with the cooler stellar wind plasma, so the profiles of specific internal energy along the beam are also almost identical. We conclude that the dissipation of kinetic energy into internal energy along the beam is essentially the same in all three mass-loaded models. Finally, the similarity of the velocity and specific internal energy profiles implies that the relativistic beam Mach number,  $\mathcal{M}$  must vary in the same way for models A, B and C. It adjusts during the first 20 pc after the injection to a value around 2.4, thereafter decreasing along the beam (Fig. 11f).

In the contrasting case of low or zero mass loading (models A0 and D), the average beam density profiles are dominated by cocoon material accelerated by shear at the interface. A comparison between the profiles for the beam in model A0 (shown in Fig. 11) and the values of the same quantities at injection (Table 1) allows us to quantify the effects of this boundary-layer entrainment. The average flow velocity of the beam is  $0.83c$ , reduced by 12% from its value of  $0.95c$  at injection. The density however increases by a factor of 70 – 100 since the shear layer material included in the jet by our definition (cells with axial velocity larger than  $0.4c$ ) dominates the average. The opposite happens in the case of the specific internal energy, which is several orders of magnitude larger in the beam than in the cocoon. The average is dominated by the beam and shows a reduction of about 30% from the injection value. Increasing the velocity cut-off in the definition of the beam reduces the beam radius and produces averages closer to the values at injection. A comparison between the density profiles for models A0 and A (Fig. 11e), confirms that mass loading by stellar winds dominates over that from shear entrainment in models A, B and C (but not in D).

We also note that the plasma in all of our models cools down along the jets because our jets are initially thermodynamically hot. This cooling is most pronounced in models A, B and C and least in A0, with D being intermediate between them. Thus, the effect of thermal dilution between the original beam plasma and the entrained stellar wind plasma dominates over the heating produced by dissipation. This is not what happens in some of the cases considered by BLK, notably their ‘cold’ reference model.

We can gain more insight into the behaviour of the jet

radius and internal density from the constraints set by mass conservation and pressure balance. Time independence of the equation of continuity requires that

$$\frac{d}{dz}(A\rho Wv) = Aq, \quad (16)$$

along the beam, where  $A$  is the beam cross section and  $\rho$ ,  $q$ ,  $v$  and  $W$  are respectively the averages across the beam of the rest-mass density, the mass-entrainment rate, the flow velocity and the Lorentz factor. Hence, the product  $A\rho$  must grow fast enough to balance the deceleration and still give a positive derivative in Eq. (16). As a result,  $\rho$ ,  $A$  or both must increase along the beam.

The pressure in the beam is governed by pressure balance with the cocoon. Since the cocoon is almost isobaric, the beam pressure profile (averaged over fluctuations due to shocks) is almost constant (Fig. 11d). This panel also shows the smaller amplitude of the internal shocks in models A, B and C, mentioned at the beginning of this section. To counterbalance the effect of the decrease in the specific internal energy and keep the pressure constant, the density must increase along the beam (Fig. 11e). In practice, both  $\rho$  and  $A$  increase to ensure pressure equilibrium and to satisfy the equation of continuity. Note that beam expansion leads to further mass loading, which in turn leads to further deceleration and cooling. The final result is an effective deceleration of the jet head in models A, B and C, and associated decollimation and flaring of the jet beyond this point (see Section 4.4). On the other hand, the triggering of this runaway process occurs only for high enough mass-loading rates: model D (with a mass-loading rate only one order of magnitude lower than that of models A, B and C) evolves in essentially the same way as the unloaded model A0.

#### 4.4 Head dynamics and jet flaring

The supersonic beam ends at a terminal shock where the beam flow decelerates and transfers part of its momentum to the ambient. In powerful jets, the head of the jet (the region between the terminal shock and the bow shock) forms a hot-spot. In the models presented here, due to the weakness of the jet, the region is quite broad and there is no substantial enhancement of the internal energy density. Fig. 12 shows the position of the terminal shock as a function of time for all of the simulations in this paper. By the end of the simulations, the terminal shock in models A, B and C has nearly stalled at about 800 pc, but those in models A0 and D are still propagating.

In these axisymmetric simulations, the growth of KH pinching modes also helps to trigger jet disruption via the process of external mass loading. Although the pressure oscillations along the jet (Fig. 11d) are larger in models A0 and D, the growth of the pinch mode surface amplitude is slower than in models A, B and C. These modes are manifest for the latter group in the large-amplitude oscillations of the averaged flow variables (beam axial flow velocity, specific internal energy, pressure, rest-mass density and Mach number) at distances between  $\approx 500$  pc and disruption (Fig. 11). The effects of pinching modes can also be seen for all of the simulations in the colour pressure panels of Figs. 4 and 6–8. From linear relativistic KH theory, Hardee (1987) and Hardee et al. (1998) showed that the growth lengths (i.e.

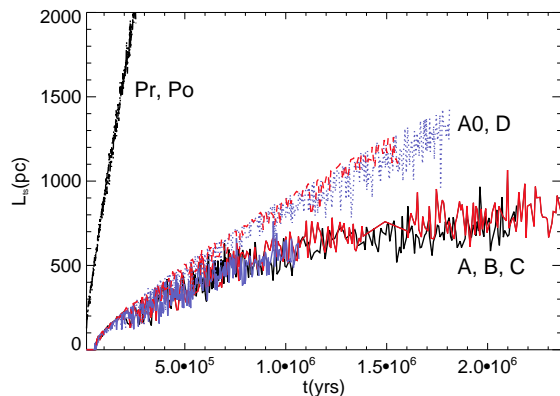


**Figure 12.** Position of the terminal shock as a function of time for all of the simulations discussed in this paper. Filled black: A; filled red: B; filled blue: C; dotted black: A0; dotted blue: D; dash-dotted black: Po; long-dashed black: Pr

the  $e$ -folding lengths of the growing modes) increase with increasing  $\mathcal{MR}$ . In the absence of deceleration due to mass loading, we would expect similar growth lengths for the beams of models A, B, C, D and A0, since they have roughly the same values of  $\mathcal{MR}$  at injection. However, the continuous deceleration and dissipation in models A, B and C cause  $\mathcal{MR}$  to decrease with distance, even though the beams expand, so the growth lengths also decrease. Moreover, at low values of  $\mathcal{MR}$ , the simple supersonic scaling breaks down and growth lengths drop rapidly. Thus, we conclude that the main cause of the relative increase in the growth rates and the earlier disruption of the jets in models A, B and C is the deceleration of the flow compared with that in A0 and D.

In order to quantify the further deceleration after jet disruption, Fig. 13 shows plots of average axial velocity against distance continuing as far as the contact discontinuity with the shocked ambient gas. We cannot adopt the definition of the beam used earlier (axial velocity  $> 0.4c$ ), as the velocities in the jet head region are too low, and have held the radius of the averaging region fixed at its value immediately before disruption. The plots therefore represent the on-axis velocity in the head region. The models with zero or low mass loading (A0 and D; Fig. 13 left panel) decelerate from  $\approx 0.8c$  just before disruption to a mean speed of  $\approx 0.3c$  over a distance of  $\approx 500$  pc, with large fluctuations. For the models including mass loading (A, B and C; Fig. 13 right panel), the beams decelerate from  $\approx 0.8c$  to  $\approx 0.5c$  before disruption and the final speed is  $\approx 0.1c$ .

#### 4.5 Transverse velocity profiles

As noted in Section 1, Laing & Bridle (2014) asserted that the development of a centrally-peaked transverse velocity profile was not consistent with mass input distributed throughout the jet volume, as would be expected for stellar mass loading. In agreement with this statement, our simulations show that, although mass load by stellar winds produces an expansion of the jet and a wide shear-layer, the inner region of the jet preserves a flat transverse velocity profile until the jet is disrupted. Profiles at 80 and 540 pc



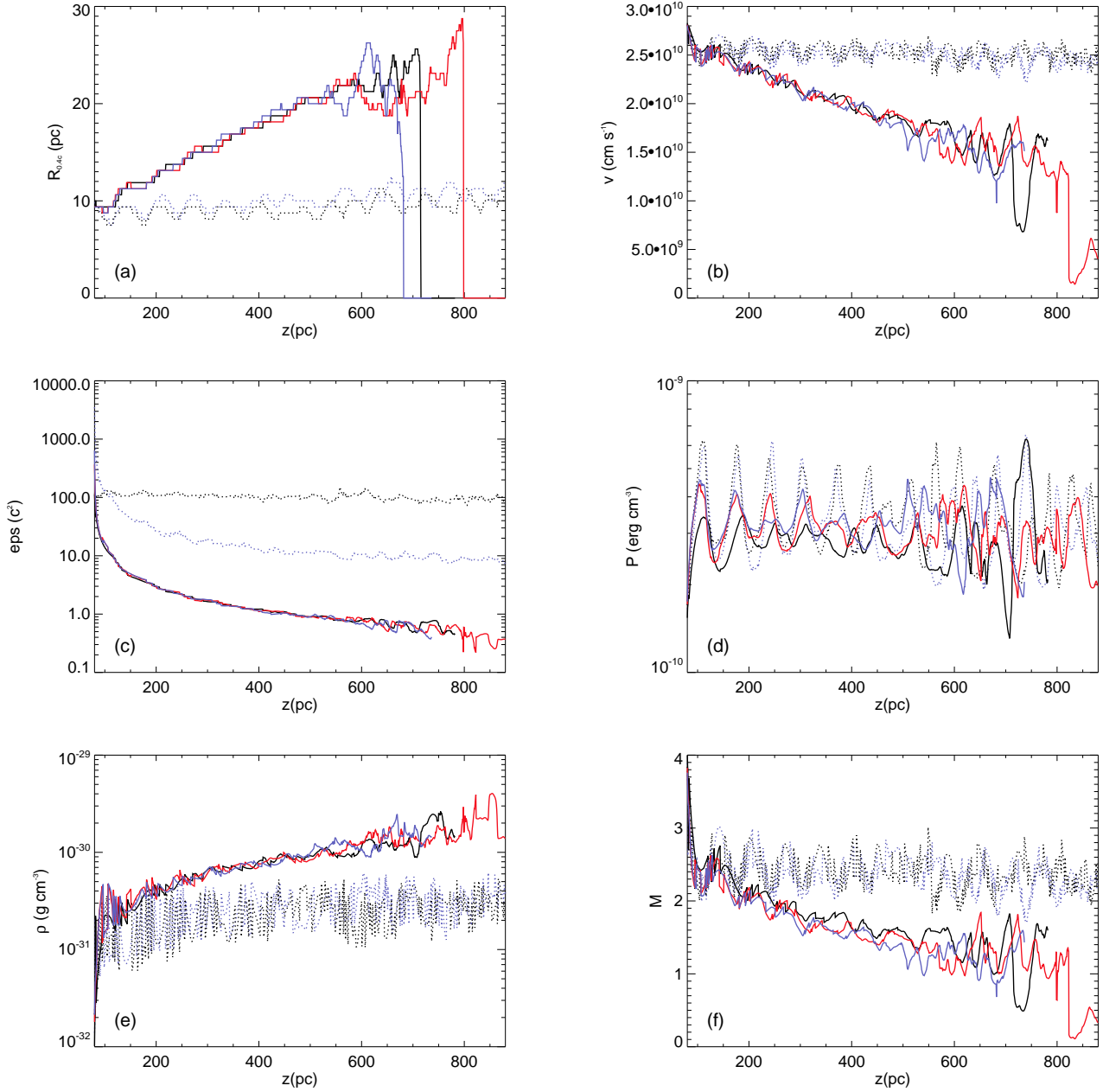


**Figure 11.** Plots of averaged beam parameters against axial distance,  $z$ , for models A, A0, B, C and D at the end of the simulation. (a) radius of the beam; (b) averaged value of axial velocity; (c) specific internal energy; (d) pressure; (e) density; (f) relativistic Mach number. Filled black: A; filled red: B; filled blue: C; dotted black: A0; dotted blue: D.

for models A and B show this effect clearly (Fig. 14). After disruption, the transverse profiles become centrally peaked, but here the deceleration is primarily due to interactions with the ambient medium rather than to stellar mass loading, and the profiles are therefore similar (although with higher central values) for models A0 and D, which have zero and low mass loading, respectively (Fig. 14).

#### 4.6 Backflow

Another interesting difference observed between the simulations with and without mass loading relates to the backflow,

with models A, B and C showing small backflow velocities,  $< 0.1 c$ , whereas models A0 and D show regions with velocities  $\simeq 0.1 c$ . The cause of this difference is related to the strength of the terminal shock, which ultimately depends on the flow velocity immediately upstream of the shock. The powerful jet simulation Pr is a more extreme case, with backflow velocities  $\simeq 0.6 c$  close to the shock (Section 3.1). In all cases, mass-loading at the contact discontinuity with the shocked ambient produced by KH instability decelerates the backflow. Recently, Laing & Bridle (2012) have claimed the detection of backflows with velocities in the range of  $0.05 - 0.35 c$  in two low-luminosity radio galaxies. If this

result is confirmed, it could be concluded from our results that the jet flow velocity at the terminal shock is still large in those radio galaxies. It is not clear, however, that the situations are analogous, since the backflows modelled by Laing & Bridle (2012) are seen around the outer regions of the jets, well downstream of the flaring region and initial deceleration.

#### 4.7 Dynamical models of FRI jets

Over the years, a model for the jets in FRI radio sources has emerged in which the main actors producing jet deceleration within the first kiloparsec are (internal) mass loading and/or strong recollimation shocks. In both cases, instabilities with post-linear or non-linear amplitudes develop farther downstream and trigger external entrainment at the edges of the jets (Bicknell 1984; Laing 1993; Komissarov 1994; Laing 1996; Laing & Bridle 2002a,b; Rossi et al. 2008, BLK, PM07). The important new result from the simulations presented here is that a low-power ( $L_j \sim 10^{41} - 10^{43} \text{ erg s}^{-1}$ ) FRI jet can be decelerated efficiently as a result of mass loading from the winds of the old stellar populations which dominate the low-excitation radio galaxies typically associated with FRI radio sources, whereas a high-power jet ( $L_j \sim 10^{44} \text{ erg s}^{-1}$ ) cannot. There must be a range of variation between individual galaxies, depending on the precise stellar distribution and population, but the basic result should be robust.

A corollary is that low-power FRI jets cannot be magnetically dominated on kiloparsec scales: the stellar mass loading will completely change the nature of the outflow within a few hundred pc. There are also important implications for the lobe dynamics of weak FRI sources and their ability to act as sources of ultra-high energy cosmic rays: Wykes et al. (2013) have recently suggested that the pressure in the lobes of Centaurus A is dominated by heated plasma originating from stellar mass input.

Other types of host galaxy may generate higher mass input rates, however. For example, high-excitation radio galaxies typically have lower stellar masses, but younger stellar populations with higher average mass-loss rates (e.g. Best & Heckman 2012). Individual young, massive stars and starbursts may also be important (Hubbard & Blackman 2006). The high-excitation radio galaxies also have broad- and narrow-line regions, which could provide mass loading sources for jets if the filling factors are large enough to cause frequent encounters between the jets and ionized gas clouds (Araudo, Bosch-Ramon & Romero 2010). Entrainment of molecular clouds into the jets is another possibility (Hardcastle et al. 2003). These sources of mass input may be able to decelerate more powerful jets, and should be investigated in future simulations.

Recollimation shocks (Section 4.3) result from the response of the jet to a large pressure imbalance with its surroundings and have been studied in the context of the collimation and structure of extragalactic jets in both classical (Sanders 1983; Falle 1991) and relativistic regimes (Wilson 1987; Daly & Marscher 1988; Komissarov 1994). If the jet is instead under-pressured or only slightly over-pressured with respect to the environment, small amplitude pinching will be induced, as observed in models A0 and D. This pinching could then couple to a KH unstable mode and grow

with distance, triggering mixing and deceleration. The spatial scale at which this process develops depends on the jet and ambient properties but, in general, will be longer than the kiloparsec scale. The most interesting case is, however, when a recollimation shock reflects on the axis in a Mach reflection rather than a regular reflection. In this case, a planar Mach disk shock is formed, decelerating the flow very efficiently and leading to a subsonic flow in the shock rest frame. Based on the significant overpressure at the flaring point in their models for 3C31, Laing & Bridle (2002b) proposed that the flaring point is associated with a stationary shock system, even though efficient Mach disks are only formed for jets with opening angles much larger than the  $8.5^\circ$  found by Laing & Bridle (2002b) for the inner region of 3C 31. In PM07, the authors tested such a possibility based on axisymmetric numerical simulations of the 3C 31 jet and environment. Three small Mach disks were produced within the 2 kpc length of the flaring region in the model jet. Although the jet simulated in PM07 was injected with a large overpressure factor of 7.8 compared with the ambient, jets generate their own environment (the cocoon), which is also overpressured. The jet was in fact only marginally overpressured with respect to its immediate surroundings and had a relatively small  $13.8^\circ$  opening angle close to injection. Nevertheless, the series of recollimation shocks was able to decelerate the flow to subsonic speeds.

With the caveats noted in Section 1, kinematic models of FRI jets (Laing & Bridle 2014) imply that deceleration from  $0.8c$  to sub-relativistic speeds is a fairly gradual process, involving the development of transverse velocity gradients and therefore associated with instabilities and boundary-layer entrainment. This leaves open the question of whether recollimation shocks provide the initial trigger for deceleration. The high-resolution observations summarized by Laing & Bridle (2014) present a challenge to the idea that deceleration is initiated by recollimation shocks, at least in the two best-resolved cases, 3C 296 and NGC 315 (their Fig. 17d and i). Firstly, neither of these jets show bright features crossing the jets at the start of their flaring regions that might plausibly be identified with strong reconfinement shocks. Instead, the brightness enhancements in the flaring region are complex, non-axisymmetric and restricted to the central parts of the jets. Secondly, the expansion rates of the jets increase monotonically with distance after the flaring point, with no sign of recollimation until much larger distances. On the other hand, the bright knot at the base of the flaring region in 3C 31 (Laing & Bridle 2014, their Fig. 17e) could still plausibly be associated with a recollimation shock. Higher-resolution observations are needed to decide whether such shocks are present in FRI jets.

Another option considered to explain the deceleration of the flow is the development of instabilities that grow to nonlinear amplitudes and could give rise to the flaring of emission. Laing & Bridle (2014) suggested that the growing modes have to be high-order because the observed jets flare without disruption. All that is really necessary, however, is that they have short wavelengths. The process of slow deceleration could, instead, be related to the type 2 unstable flows (UST2) classified by Perucho et al. (2005). These occupy a characteristic location in the relativistic Mach number - Lorentz factor plane and were confirmed using three-dimensional simulations by Perucho et al. (2010).

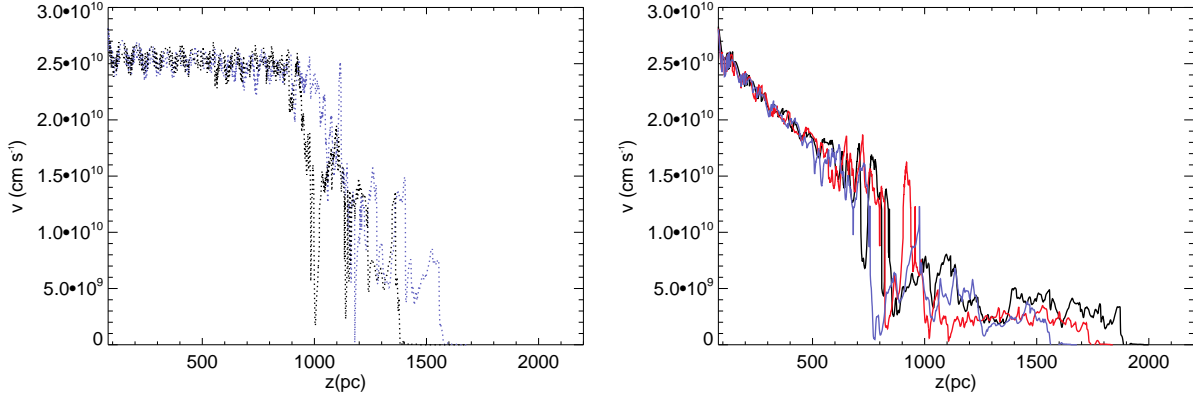


**Figure 13.** Profiles of average axial velocity covering the full simulation length. Upstream of the jet disruption point, these are exactly as plotted in Fig. 11. In the post-disruption region, the radius of the jet is held constant at its value immediately before disruption. Left panel: models A0 (blue) and D (black). Right panel: models A (black), B (red) and C (blue).

This type of deceleration corresponds to a slow and progressive mixing, expansion and deceleration of jets that is caused by short-wavelength, but low-order, body modes. Perucho et al. (2005) showed that this mechanism can be relevant in hot jets, because the linear solutions give high growth-rates and short wavelengths for the resonant values of KH body-modes, as opposed to the solutions obtained for colder jets. Interestingly, Laing & Bridle (2014) conclude that the jets in their sample could be formed by hot, low-Mach-number flows. Further work is needed to establish whether this mechanism is effective for the parameter range applicable to FRI jets. The resolution used in our simulations is not high enough to allow for the development of short-wavelength unstable modes. However, the goal of this paper is to determine the range of jet powers over which mass-loading by stars could be relevant. Our simulations allow us to achieve this goal and also to demonstrate the development of longer wavelength unstable modes. A detailed study to compare the effects of the growth of short-wavelength modes and mass-loading by stars would require specific high-resolution simulations.

It is important to note that the growth of instabilities from the linear regime requires pressure equilibrium with the ambient: if the jet is overpressured and expands, the expansion dominates the interaction between the jet and the ambient, making it difficult for a growing instability to become dynamically important. In addition, the wavelength of the fastest-growing modes changes proportionally to the jet radius and the growth rates are reduced (see, e.g., Hardee 1987, 2000, 2011).

We stress that our simulations have followed the evolution of the propagating jets for  $\lesssim 2 \times 10^6$  yr after they are initiated. Although we believe that the simulations capture several important aspects of jet propagation, the resulting morphologies are very different from those observed in old FRI sources. Although the head of the jet in the decelerated models advances at a very low velocity by the end of the simulation, the shape and structure of the cocoon are likely to change radically when the bow-shock expands in the strong pressure gradient beyond the galactic core. The spherical structure observed around the injection region is expected to cool and become denser as the surrounding material falls

back towards the galactic centre and is entrained across the contact discontinuity. This spherical cocoon might be observable in young, low-power radio sources, but it is likely to disappear at later times due to mixing with the colder and denser material that surrounds it. Three-dimensional, long-term simulations should be performed to study the transition between the early stage studied here and the evolution of the whole structure when the bow-shock propagates out of the galactic core and becomes transonic.

## 5 SUMMARY AND CONCLUSIONS

We have performed a series of axisymmetric simulations of the early evolution (up to  $2 \times 10^6$  yr) of FRI jets in a realistic galactic environment to investigate the effects of mass loading by stellar winds. The simulations presented here allow us to capture the effects of mass loading on beam evolution within the host galaxy and are precise enough to discriminate between models differing by a factor of ten in the mass entrainment rate. Our results are consistent with previous steady state simulations (BLK) and theoretical estimates (Hubbard & Blackman 2006).

The overall structure and dynamics of the cocoon-shocked ambient system is very similar for all models with the same power and thrust. Slight differences in long-term evolution result from differences in the dynamics of the jet head (which are affected by the mass loading). The mass load carried by the beam affects its internal structure (internal shocks, pinching, beam radius and jet opening angle) and properties (increase in the rest mass density, cooling and deceleration).

We find that mass entrainment rates consistent with present models of stellar mass loss in elliptical galaxies lead to deceleration of the beam plasma and effective decollimation of weak ( $L_j \sim 10^{41} - 10^{42}$  erg s $^{-1}$ ) FRI jets on scales of about 1 kpc. Deceleration is accompanied by expansion and, in axisymmetric simulations, the development of disruptive pinch modes that lead to the decollimation and further deceleration of the jet due to external entrainment. The composition of the jet is also completely changed by the process of mass loading, ruling out a dominant magnetic field



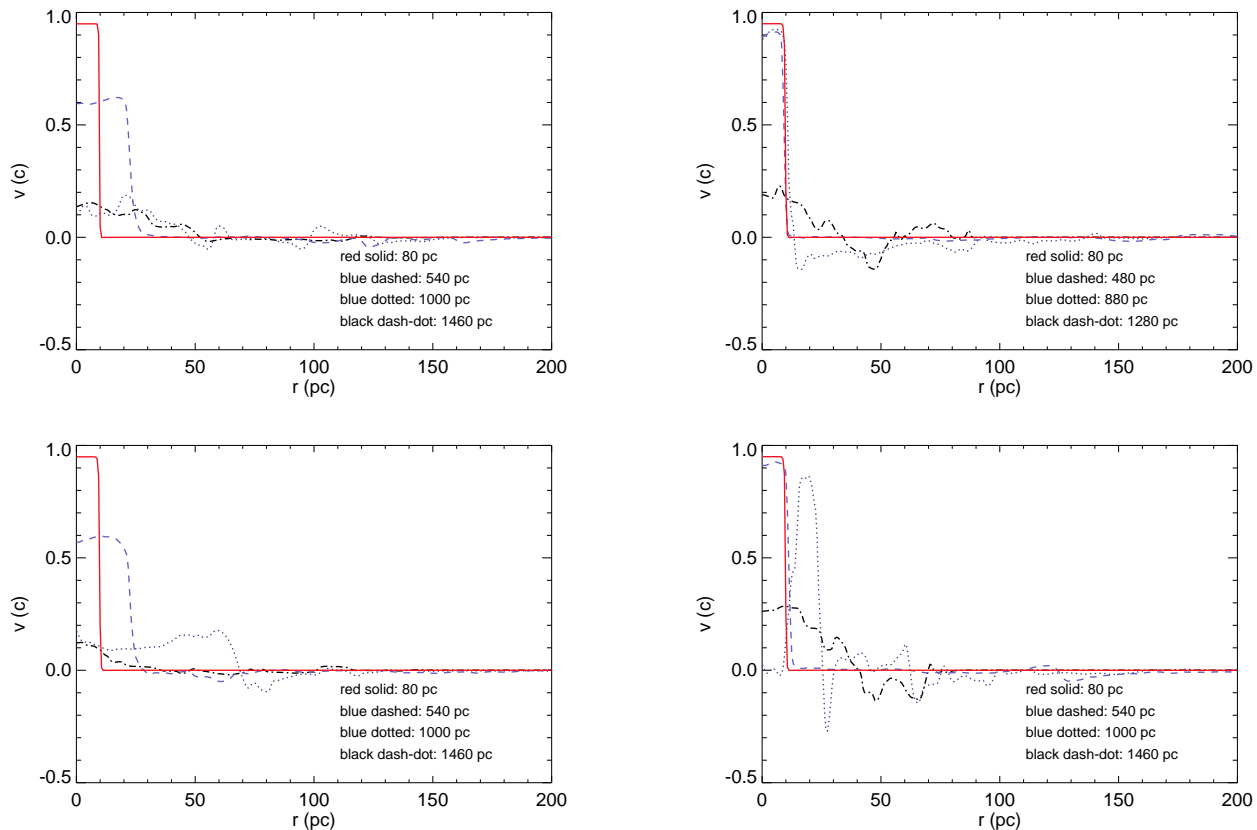


**Figure 14.** Radial cuts of axial velocity at different positions along the axial direction, typically at the injection position, one quarter, one half, and three quarters of the simulated grid in each case. The top left panel shows model A, the top right panel shows model A0, the bottom left panel shows model B, and the bottom right panel shows model D. The order of the lines, starting from the injection is: red solid, blue dashed, blue dotted, and black dash-dotted.

on kiloparsec scales in low-power FRI jets. However, stellar mass loading seems to be unable to decelerate the most powerful ( $L_j \gtrsim 10^{43} \text{ erg s}^{-1}$ ) FRI jets. In these powerful jets, the formation of strong recollimation shocks when the pressure in the environment drops well below that of the jet or continuous mass entrainment produced by short-wavelength KH body modes, are more plausible mechanisms for deceleration, entrainment and mixing (see also Laing & Bridle 2014). Future work should include high-resolution three-dimensional simulations to allow for a detailed comparison between the different proposed mechanisms of deceleration. Our conclusions can also be tested observationally by modelling larger samples of weak and powerful FRI jets using the techniques developed by Laing & Bridle (2014). We would expect transverse velocity gradients to develop in the powerful jets, but the weak jets should maintain their initial transverse velocity profiles as they decelerate.

## ACKNOWLEDGMENTS

MP and JMM acknowledge financial support by the Spanish “Ministerio de Ciencia e Innovación” (MICINN) grants AYA2010-21322-C03-01, AYA2010-21097-C03-01 and CONSOLIDER2007-00050, and by the “Generalitat Valenciana” grant “PROMETEO-2009-103”. PEH acknowledges

support from NSF award AST-0908010 and NASA award NNX08AG83G to the University of Alabama. MP and JMM acknowledge Joan Ferrando for interesting discussions at the start of this project.

## REFERENCES

- Araudo A.T., Bosch-Ramon V., Romero G., 2010, *A&A*, 522A, 97
- Asada, K., Nakamura, M., 2012, *ApJL*, 745, 28
- Best P.N., Heckman T.M., 2012, *MNRAS*, 421, 1569
- Binney J., Merrifield M., 1998, *Galactic Astronomy* (Princeton: Princeton University Press)
- Bicknell G.V., 1984, *ApJ*, 286, 68
- Bicknell G.V., 1994, *ApJ*, 422, 542
- Bowman M., Leahy J.P., Komissarov S.S., 1996, *MNRAS*, 279, 899 (BLK)
- Carilli C.L., Barthel P.D., 1996, *A&ARv* 7, 1
- Celotti A., Ghisellini G., 2008, *MNRAS*, 385, 283
- Croston J.H., Hardcastle M.J., Birkinshaw, M., Worrall, D.M., Laing, R.A., 2008, *MNRAS*, 386, 1709
- Daly R.A., Marscher A.P., 1988, *ApJ*, 334, 539
- De Young D.S., 1986, *ApJ*, 307, 62
- De Young D.S., 1993, *ApJ*, 405, L13
- Faber S.M., Gallagher J., 1976, *ApJ*, 204, 365

- Falle S.A.E.G., 1991, MNRAS, 250, 581
- Fanaroff B.L., Riley J.M., 1974, MNRAS, 167, 31
- Giovannini G., Cotton W.D., Feretti L., Lara L., Venturi T., 2001, ApJ, 552, 508
- Hardcastle M.J., Worrall D.M., Birkinshaw M., Laing R.A., Bridle A.H., 2002, MNRAS, 334, 182
- Hardcastle M.J., Worrall D.M., Kraft R.P., Forman W.R., Jones C., Murray S.S., 2003, ApJ, 593, 169
- Hardee P.E., 1987, ApJ, 313, 607
- Hardee P.E., 2000, ApJ, 533, 176
- Hardee P.E., 2011, in Romero, G., Sunyaev, R. and Belloni, T., eds., IAU Conference Series 275, IAU Symposium 275: Jets at all Scales, p. 41
- Hardee P.E., Rosen A., Hughes P.A., & Duncan G.C., 1998, ApJ, 500, 599
- Hubbard A., Blackman E.G., 2006, MNRAS, 371, 1717
- Komissarov S.S., 1994, MNRAS, 269, 394
- Laing R.A., 1993, in Burgarella D., Livio M., O’Dea C. P., eds., Space Telescope Science Institute Symposium Series, Astrophysical Jets. STScI, Baltimore, Cambridge Univ. Press, Cambridge, p. 95
- Laing R.A., 1996, in Hardee P.E., Bridle A.H., Zensus J.A., eds., Energy Transport in Radio Galaxies and Quasars. Proceedings of the 175th IAU Symp., Kluwer, Dordrecht, p. 147
- Laing R.A., Bridle A.H., 2002a, MNRAS, 336, 328
- Laing R.A., Bridle A.H., 2002b, MNRAS, 336, 1161
- Laing R.A., Bridle A.H., 2012, MNRAS, 424, 1149
- Laing R.A., Bridle A.H., 2014, MNRAS, 437, 3405
- Lauer T.R., et al., 2007, ApJ, 664, 226
- Meliani Z., Keppens R., Giacomazzo B., 2008, A&A, 491, 321
- Meyer E.T., Fossati G., Georganopoulos M., Lister M.L., 2011, ApJ, 740, 98
- Müller, C., Kadler, M., Ojha, R., et al., 2011, A&A, 530, L11
- Perucho M., Martí J.M., Hanasz M., 2005, A&A, 443, 863
- Perucho M., Martí J.M., 2007, MNRAS, 382, 526 (PM07)
- Perucho M., Martí J.M., Cela, J.M., Hanasz, M., de la Cruz, R. Rubio, F., 2010, A&A, 519, A41
- Phinney E.S., 1983, PhD thesis, University of Cambridge
- Rossi P., Mignone A., Bodo G., Massaglia S., Ferrari A., 2008, A&A, 488, 795
- Sanders R.H., 1983, ApJ, 266, 73
- Synge J.L., 1957, The Relativistic gas (Amsterdam: North-Holland publishing Company)
- Wang Y., Kaiser C.R., Laing R., Alexander P., Pavlovski G., Knigge C., 2009, MNRAS, 397, 1113
- Wilson M.J., 1987, MNRAS, 226, 447
- Wykes S. et al., 2013, A&A, 558A, 19